Materials Science and Engineering A369 (2004) 124–137

www.elsevier.com/locate/msea

Studies of the microstructure and properties of dense ceramic coatings produced by high-velocity oxygen-fuel combustion spraying

A. Kulkarni [a,*], J. Gutleber [a], S. Sampath [a], A. Goland [a], W.B. Lindquist [a], H. Herman [a], A.J. Allen [b], B. Dowd [c]

[a] *Department of Materials Science and Engineering, State University of New York, Stony Brook, NY 11794-2275, USA*
[b] *Ceramics Division, National Institute of Standards and Technology, Gaithersburg, MD, USA*
[c] *Brookhaven National Laboratory, Upton, NY, USA*

Received 24 July 2003; received in revised form 22 October 2003

Abstract

High-velocity oxygen-fuel (HVOF) spraying stands out among the various processes to improve metal and ceramic coating density and surface characteristics. This paper explores microstructure development, coating characterization and properties of HVOF sprayed alumina coatings and compares these with those produced using the conventional air plasma spray process. We report on the characterization of these coatings using small-angle neutron scattering (SANS) and X-ray computed microtomography (XMT) to explain the behavior observed for the two coating systems. Microstructure information on porosity, void orientation distribution, void mean opening dimensions and internal surface areas have been obtained using SANS. XMT (X-ray synchrotron microtomography) has been used to nondestructively image the microstructural features in 3D at a 2.7-μm spatial resolution over a 2–3 mm field of view. 3D medial axis analysis has been used for the quantitative analysis of the coarse void space in order to obtain information on the porosity, specific surface area, pore connectivity and size distribution of the larger voids in the coatings. The results reveal different pore morphologies for the two spray processes. While only globular pores are imaged in the plasma sprayed coatings due to the spatial resolution limit, highly layered porosity is imaged in the HVOF coating. When the quantitative SANS and XMT information are combined, the different thermal and mechanical properties of the two different coating types can be explained in terms of their distinctly different void microstructures.

Keywords: Porosity; Thermal conductivity; Elastic modulus; Microstructure; Coatings; Small angle neutron scattering; Computed microtomography

1. Introduction

DC-arc plasma spray is an established process for depositing a wide range of oxide ceramics, including alumina for wear resistance and zirconia-based materials for thermal barrier coatings [1–4]. The high temperature (enthalpy) availability within the thermal plasma enables melting, relatively high-velocity delivery and deposition of ceramics onto a variety of substrates. Typically, plasma sprayed coatings contain some degree of porosity, in the form of interlamellar pores resulting from the rapid solidification of the lamellae, very fine voids formed either by incomplete inter-splat contact or by particles not melting, and thermal stress relaxation cracks [5–7]. Although, this porosity is beneficial for thermal barrier applications because it reduces the coating thermal conductivity, it is deleterious for wear and corrosion applications. The advent of high velocity oxygen-fuel (HVOF) thermal spray has made a significant impact on the field, producing dense, well-adhered deposits of metals and cermets [8]. However, there has been only limited effort in understanding and developing the process for ceramics. The limited utility for HVOF of ceramics is the relatively low temperature of the combustion flame.

The HVOF process is an enhancement of combustion spraying, in which, a compressed flame undergoes free expansion upon exiting the torch nozzle, thereby experiencing a dramatic gas acceleration [9,10]. By axially injecting the feedstock powder, the particles are also subjected to a high acceleration to supersonic velocities. Upon impacting the substrate, they spread out thinly to form a well-bonded dense

* Corresponding author. Tel.: +1-631-632-4511; fax: +1-631-632-8440.
E-mail address: anand.kulkarni@sunysb.edu (A. Kulkarni).

0921-5093/$ – see front matter © 2003 Elsevier B.V. All rights reserved.
doi:10.1016/j.msea.2003.10.295

coating [11,12]. In recent years, advanced HVOF torches have become available, based on converting the high particle kinetic energy into thermal energy on impact causing the particles to melt, leading to acceptable ceramic deposition efficiencies (~50% or more). The use of fine ceramic powders, together with an appropriate nozzle design, allows the deposition of alumina-based ceramics, $BaTiO_3$, etc. The deposits are characterized by very high densities, excellent adhesion and smooth surface profiles. However, limited information exists on the imperfection characteristics of these deposits. The technological potential of HVOF warrants an examination of this process and the associated materials properties, which is the subject of this paper. While small-angle neutron scattering (SANS) methods have been used previously to characterize/quantify the anisotropic nature of thermal sprayed ceramic coatings [13–15], the X-ray computed microtomography (XMT) technique has only been explored recently to visualize gross porosity in these coatings [16].

This paper compares the processing influences on alumina coatings between plasma spraying with those for HVOF spraying. The emphasis is on the microstructure development and on coating performance. The influence of in-flight particle behavior on phase composition and microstructure characteristics is presented. It is clear that, for both processes, sufficient melting occurs in-flight to achieve well-formed splats, and that porosity, pore size distribution and adhesion are the factors, which dominate the coating system behavior. Quantitative microstructural characterization, carried out by combining SANS and XMT, is presented to establish the processing—microstructure—property correlations. The results reveal differences in the pore morphologies for the two spray processes. A relative predominance of globular pores in plasma sprayed deposits is replaced by coarse layered porosity in HVOF deposits. A comparison of the measured in-plane and through-plane properties of the coatings reveals the significance of the layered pore structure in HVOF deposits.

2. Experimental procedure

2.1. Deposition parameters

The plasma sprayed coatings were deposited using a Sulzer Metco 3MB[1] plasma gun using an Ar/H_2 gas combination. The HVOF-spray coatings were deposited using a Praxair HV2000[1] torch using propylene as the fuel gas. The feedstock characteristics were different for the two cases to allow for the different melting characteristics within a high-temperature plasma compared to those within a combustion flame. As indicated in Table 1, a small particle size was required in the HVOF case in order to give sufficient heating of the material to ensure melting and efficient deposition. The industrially-relevant spray parameters are listed in Table 2. The in-flight particle diagnostics were measured using a Tecnar DPV2000* system which monitored particle temperature and velocity, as shown in Table 3.

The coatings were deposited onto grit-blasted mild steel substrates. Single splats were collected and observed by optical microscopy, since droplet–substrate interactions govern much of the deposit's integrity and properties. Microstructural evaluation was carried out using optical microscopy and scanning electron microscopy (SEM) of the cross-sections of the coatings along with X-ray diffraction (XRD) for phase composition. Freestanding coatings (1 mm thick) were used for porosity characterization by SANS and XMT. In fact, information on porosity was sought by four techniques. While only surface-connected porosity was measured by mercury intrusion porosimetry (MIP) using a Quantachrome Autoscan 33* porosimeter, the XMT studies allow detection of both open and closed porosity. However, spatial resolution issues preclude detection of all of the porosity in the system. Therefore, the total porosity content is determined using the precision density (PD) method, where mass-over-volume ratios were obtained for a cut rectilinear

Table 1
Feedstock characteristics of the alumina powders

Manufacturer	Process	Powder type	Size distribution
Praxair	HVOF	Agglomerated and sintered	−22 μm + 5 μm
Vista	Plasma	Sol–gel processed	−55 μm + 15 μm

Table 2
Deposition parameters

Spray torch	
Plasma	Metco 3 MB
Voltage (V)	68–71
Current (A)	550
Primary gas (Ar) (SLM)	40
Secondary gas (H_2) (SLM)	8
Carrier gas (Ar) (SLM)	4
Standoff (mm)	100
Feed rate (g/min)	20–30
HVOF	Praxair HV2000
Propylene (SLM)	75
Oxygen (SLM)	273
Nitrogen (SLM)	21
Combustion chamber (mm)	22
Standoff (mm)	150
Feed rate (g/min)	20–30

Table 3
In-flight diagnostics with measured standard deviations

Process	Plasma	HVOF
Temperature (°C)	2376 ± 300	2100 ± 200
Velocity (m/s)	65 ± 50	680 ± 50

[1] Information on commercial products is given for completeness and does not necessarily constitute or imply their endorsement by the National Institute of Standards and Technolog.

specimen. The porosity obtained using this technique is input into the SANS/MSANS model analysis to get quantitative separation of component porosities of the three void systems in the coating. This accounts for both the open and closed porosity of the coatings, in this case 1 mm thick. The porosity values from MIP (surface-connected porosity) and XMT (limited resolution) techniques are therefore lower. This PD technique gives the density as a percentage fraction of the maximum theoretical density (100% TD) from which the total porosity is deduced. The uncertainty in the measured density has a standard deviation ±0.1% TD, based on the average of ten measured identical specimens and an assumed theoretical density of 3.97 g/cm^3.

2.2. Coating properties

The two coating properties most sensitive to microstructure of these coatings are their thermal conductivity and elastic modulus. Therefore, in-plane and out-of-plane measurements were carried out to examine the effects of the different anisotropic coating microstructures on these properties.

Thermal conductivity measurements were carried out on a 12.5 mm (0.5 in.) diameter disk, coated with carbon on both surfaces, using a Holometrix laser flash* thermal diffusivity instrument. In this test, the sample is irradiated uniformly on one side using a single laser beam pulse (1.06 μm wavelength). The temperature rise on the other side is recorded as a function of time using an HgCdTe infrared detector (2–5.5 μm wavelengths). The recorded temperature-rise data, with allowance for the measured sample thickness, are used to calculate the thermal diffusivity directly. Also, the magnitude of the temperature rise of an unknown sample can be used to give the specific heat when comparison is made to a known reference sample. Knowledge of the bulk density, together with the thermal diffusivity and specific heat, allows determination of the thermal conductivity [17]. While "conventional" out-of-plane thermal conductivity measurement involves measurement of the temperature rise on the rear face of a sample, as shown in Fig. 1A, an in-plane measurement requires a different experimental setup [18]. For the in-plane measurements, the laser beam is collimated or focused on the front face of the sample, and the distance that heat must flow is significantly greater. A mask with a circular pinhole concentric with the beam axis is used to define the viewing radius of the IR detector.

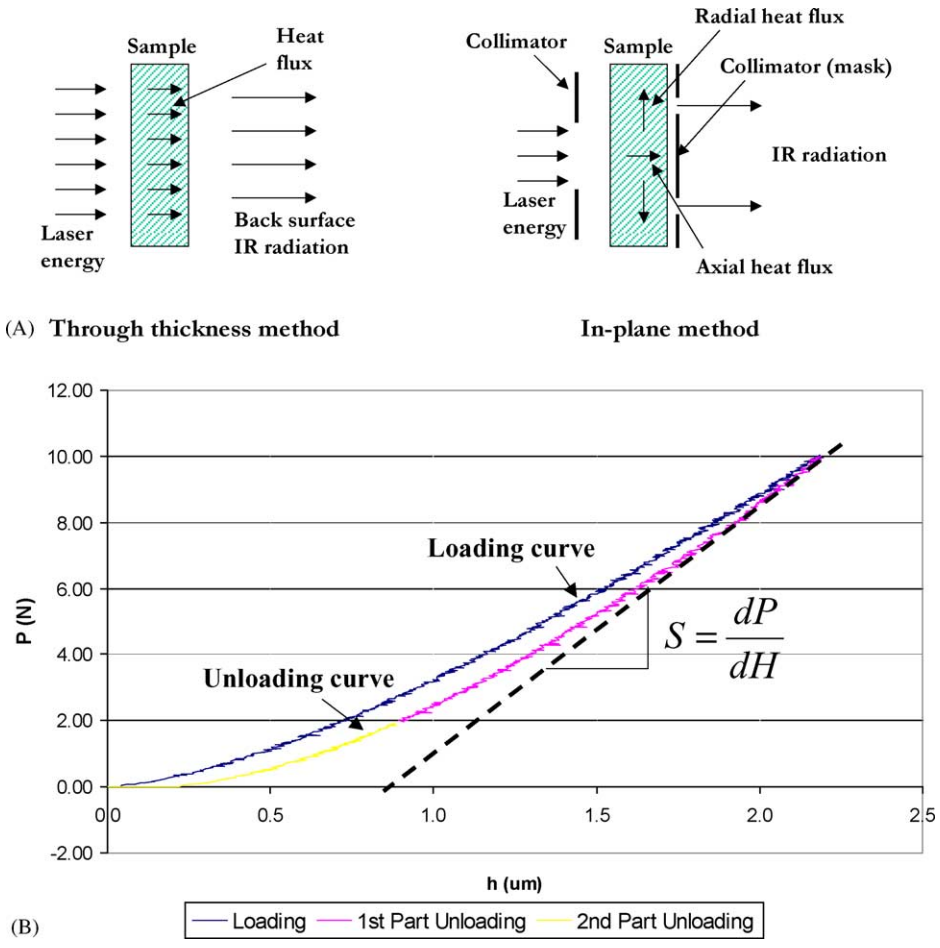

Fig. 1. (A) Schematic of a thermal conductivity set-up for two orientations and (B) analysis of a load–displacement curve for elastic modulus calculation.

Elastic modulus measurements were carried out on polished top-surfaces and cross-sections of the coatings bonded to the substrate. In this technique, depth-sensitive indentation methods extract the materials properties using the contact response of a small volume of material. In the present study, a spherical indenter was used. Continuous measurements of load/displacement curves were performed with a Nanotest 600* (Micro Materials Limited, Wrexham Technology Park, Wrexham, LL 137YP, UK) instrument using a 1.56 mm (1/16 in. WC–Co spherical indenter with a maximum load of 10 N. The instrument enables a basic load/displacement curve to be obtained, or multiple partial load/unload cycles to be performed. This allows hardness and elastic modulus values to be measured as a function of the load/contact stress. The indentation procedure employed usually consists of 10–15 loading/unloading cycles. The maximum loads of each cycle are equally divided between zero and the total maximum load. Here, partial unloading to 80% of the maximum load was used. In all tests the actual zero load was set to 0.2 mN. The load–displacement records were evaluated based on the Oliver and Pharr method [19]. An example of a load displacement curve is depicted in Fig. 1B. The elastic modulus was determined from the elastic recovery part of the unloading curve, which relates the modulus, E, to the initial loading stiffness, S, as follows:

$$S = \frac{\mathrm{d}P}{\mathrm{d}h} = \frac{2}{\sqrt{\pi}} E_\mathrm{r} \sqrt{A_\mathrm{r}}, \tag{1}$$

where E_r is the reduced elastic modulus and A_r is the area projection perpendicular to the direction of the elastic deformation. The reduced modulus is related to the true sample modulus by:

$$\frac{1}{E_\mathrm{r}} = \frac{1-\nu^2}{E} + \frac{1-\nu_\mathrm{i}^2}{E_\mathrm{i}} \tag{2}$$

where E and ν are the true Young's modulus and Poisson's ratio for the specimen and E_i and ν_i are the corresponding values for the indenter diamond.

2.3. Small angle neutron scattering

Small-angle neutron scattering studies were carried out using the NIST/NSF 30 m SANS instrument at the Cold Neutron Research Facility at the National Institute of Standards and Technology, Gaithersburg, MD [20,21]. In this experiment, a monochromatic beam of cold neutrons passes through the specimen in transmission geometry and the scattered neutrons are recorded on a two-dimensional detector (Fig. 2). The details of the experiment are described elsewhere [13–15]. The voids and grains within the sample have different neutron scattering length densities, ρ, causing a small component of the incident beam to be scattered. The SANS experiments comprise two types of measurements, the first being anisotropic Porod scattering, where the variation, with sample and beam orientation, in the intensity of the terminal slope of the small-angle scattering at large scattering angles can be related to the

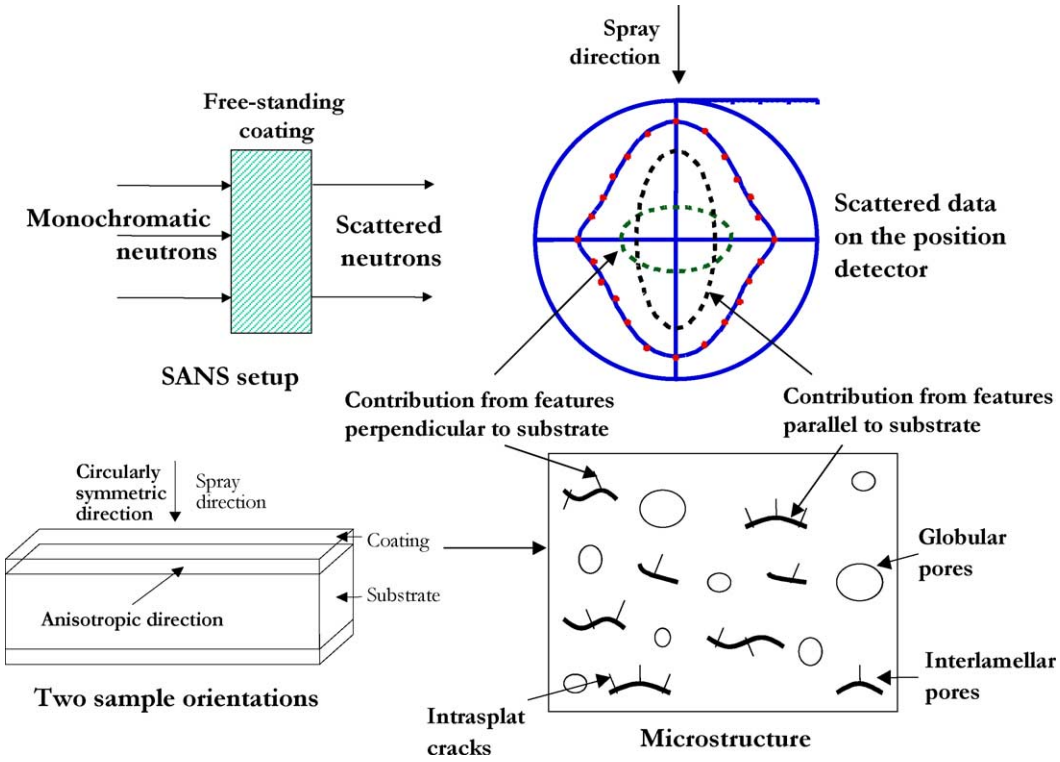

Fig. 2. SANS experimental set-up and model representation.

anisotropic void surface area distribution. Upon averaging the Porod scattering over all sample orientations, the total void surface area per unit sample volume is obtained, independent of the precise void morphology present. The fine features in the microstructure are the dominant contributors to this total surface area. The second type of measurement is anisotropic multiple SANS (MSANS), which involves a measurement of the beam-broadening due to anisotropic multiple scattering at long neutron wavelengths. The multiple scattering usually arises from coarse features in the microstructure. The large features are the globular pores, which contribute to multiple scattering in SANS and also are imaged in XMT. The microcrack related features are the fine features in the coatings and contribute to surface area so they get accounted for only in the SANS data due to limited resolution of the XMT technique. The MSANS beam-broadening (r_c) versus wavelength for two sample orientations, with the incident beam out-of-plane (in the spray direction) and with it in-plane (i.e. in the substrate plane), yields information on the microstructural anisotropy. The sector-averaged anisotropic MSANS data also provide microstructural orientation information, as discussed elsewhere [14,15].

In Porod scattering, the scattering intensity, $I(Q)$, is a function of both the magnitude, Q, and the direction of the scattering vector, $\boldsymbol{Q}$, and its orientational average, $\langle I(\boldsymbol{Q})\rangle$ is given by:

$$\langle I(Q)\rangle \approx \frac{2\pi|\Delta\rho|^2 S_T}{Q^4}, \tag{3}$$

where $|Q| = [4\pi/\lambda]\sin\theta$, 2θ is the scattering angle, λ the wavelength, S_T the total surface area per unit sample volume and $|\Delta\rho|^2$ is the scattering contrast between the voids and the solid matrix.

More complete microstructural information is obtained by combining MSANS measurements for different sample orientations, anisotropic Porod surface area analysis, and total porosity precision density measurements. A three-component void model (interlamellar pores, intrasplat cracks and globular pores) is used to obtain quantitative information regarding the component porosities, sizes and orientation distributions. For interpretation of the anisotropic MSANS beam-broadening data, the interlamellar pores and intrasplat cracks are considered to comprise two space-filling networks of oblate spheroids, each with a fixed aspect ratio, β, while the globular pores are assumed to be spheres. Since the cracks are generally finer than the interlamellar pores, the aspect ratio for the cracks is set to a smaller value (more oblate) than for the interlamellar pores. The following four constraints are imposed in the model analysis within the limits set by the experimental uncertainties: [14,15].

(1) The component porosities must sum to the total porosity obtained from precision density measurements.
(2) The component surface areas must sum to the total surface area obtained from the orientationally-averaged anisotropic Porod scattering.
(3) The circularly-averaged MSANS beam broadening versus wavelength model predictions must be consistent with the experimental data for both sample orientations: with the incident beam out-of-plane (parallel to the spray direction), and with the incident beam in-plane (in the substrate plane).
(4) The predicted MSANS anisotropy must be consistent with that observed with the incident beam in-plane.

With these constraints, it is possible to determine the volume-weighted mean opening dimensions of the intrasplat cracks and interlamellar pores, their approximate orientation distributions with respect to the spray direction, together with the mean diameter of the globular pores. The component porosity and surface area contributions may also be distinguished.

2.4. Computed microtomography

Synchrotron X-ray XMT was carried out at the X27A beam-line at the National Synchrotron Light Source, Brookhaven National Laboratory, Brookhaven, NY [22,23]. In this experiment, a highly-collimated, large-area, X-ray synchrotron beam traverses the sample. The beam transmitted through the sample is recorded on a scintillator area detector, which converts the X-ray attenuation map into a visible image. The XMT technique provides volumetric data of elemental composition by mapping the 3D X-ray absorption throughout the sample. Data, in the form of cross-sectional maps of linear attenuation coefficient, are collected with the 2D detector array, such that each slice corresponds to data collected in one row of pixels. The sample is rotated, by discrete angular intervals, through 180°, about an axis perpendicular to the incident beam direction. For each view, the transmission of each ray through the sample, along a line from the source to the detector is recorded at each detector pixel position. This represents a line integral of the attenuation coefficients along this ray direction. The detector data for each view are then reconstructed using a fast filtered back transform (FFBT) algorithm to reconstruct horizontal slices, and are then stacked to build 3D images of the microstructural features at 2.7 μm resolution.

Currently, 3D medial axis transforms are being exploited in the analysis of the geometric structure of void space in porous media to obtain information on porosity, pore connectivity and size distribution [24]. The medial axis transform is a dimensional reduction of an object to its skeletal remnant, preserving information on extent and connectivity of the original object. Intuitively, a medial axis is the skeleton of an object along its geometric middle (a point for a sphere and a line along the center for a cylinder). The analysis involves thresholding an overlapping bivariate mapped distribution of attenuation coefficients (tomographic raw

images) to obtain segmented (black and white) images. This is followed by construction of the medial axis with an iterative erosion procedure [25] to trace the fundamental geometry of the void pathways. Information on porosity, pore size distribution and connectivity is obtained using numerical algorithms, the details of which are presented elsewhere [26,27].

3. Results and discussion

In this section, the experimental SANS and XMT results are presented, together with the phase and other microstructure characterizations. The microstructures are then related to the thermal and mechanical properties. Regarding phase analysis, Fig. 3 shows X-ray diffraction results for both the as-received powders (exclusively α-Al_2O_3 phase) and the deposited coatings. Due to rapid solidification, the coatings consist predominantly of γ-Al_2O_3 phase. Quantitative analysis was carried out after profile-corrections (background subtraction, smoothing and $K\alpha_2$ correction) were made on the raw data [28]. The ratio of the area under the maximum intensity peak (I_{100}) ([1 1 3] for the α-phase and [4 4 0] for the γ-phase) was used to determine the ratio of the α to γ content. The results show the HVOF deposited coating to be a mixture of 75% γ and 25% α-phase, compared to the plasma deposited coating, which is 80% γ and 20% α.

During the spraying of either coating system, the deposit is generated by successive impingements of molten droplets. Hence, particle velocity and temperature play a key role in microstructure development. In-flight particle temperatures recorded at 150 mm from the nozzle exit, equivalent to the substrate standoff distance in the case of HVOF spraying, are about 2100 °C, suggesting sufficient particle softening or melting for adhesion to the substrate. In the images in Fig. 4, the ceramic particles clearly appear to have been molten or semi-molten upon impingement. Since velocities recorded for the HVOF process are an order of magnitude greater than for the plasma spray process, significant differences in microstructure are expected. The particle impact at high velocity results in more uniform particle flattening, thus we expect a higher number of flat interfaces per unit length normal to the substrate. A smaller degree of fragmentation of the splats than in plasma-spray is observed due to the fine particle size. The splats are thin and translucent and do not show the typical mud cracking seen in plasma sprayed ceramic splats (Fig. 4a). Quantitatively, the mean splat thickness (±standard deviation) deposited in the HVOF process is $0.7 \pm 0.2\,\mu m$, while that in the plasma spray process is $2.9 \pm 0.4\,\mu m$. Also the average surface roughness (R_a) of the splats is $0.4 \pm 0.1\,\mu m$ for HVOF and $1.1 \pm 0.2\,\mu m$ for plasma spray. Such factors control the coating adhesion and development.

SEM micrographs of the two coatings are presented in Fig. 5 along with the MIP surface connected porosity and the average coating surface roughness. The microstructures show distinctive features with the plasma sprayed coating displaying large globular pores, interlamellar pores and cracks, whereas the HVOF coating shows well-adhered splats with finer porosity. High magnification images (Fig. 5c and d) show the detailed coating buildup for both cases. The microstructure shows the columnar structure within the individual splats for plasma spray, indicative of complete melting, while HVOF exhibits a compact coalescence of semi-solid splats. The Fig. 5 also reveals an additional fine-level white contrast for all of the coatings studied.

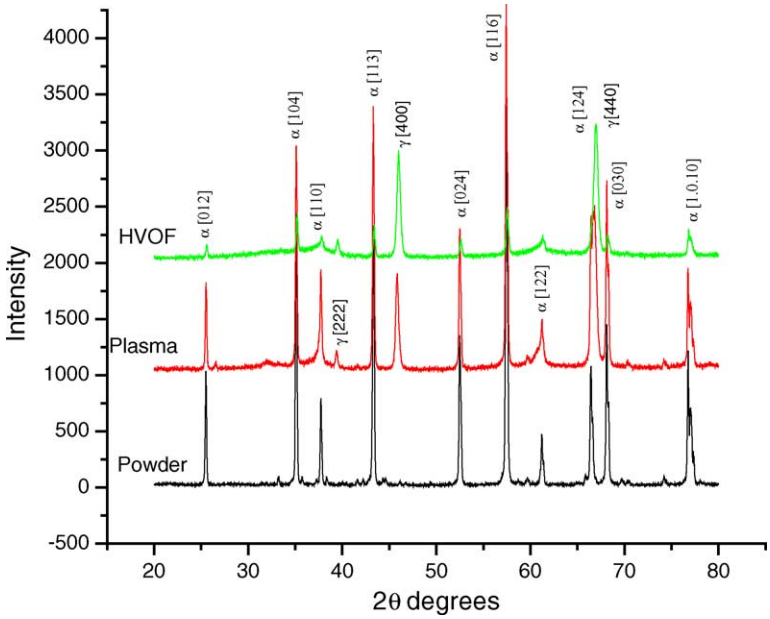

Fig. 3. X-ray diffraction data for starting α-alumina powders compared with plasma sprayed and HVOF deposited coatings.

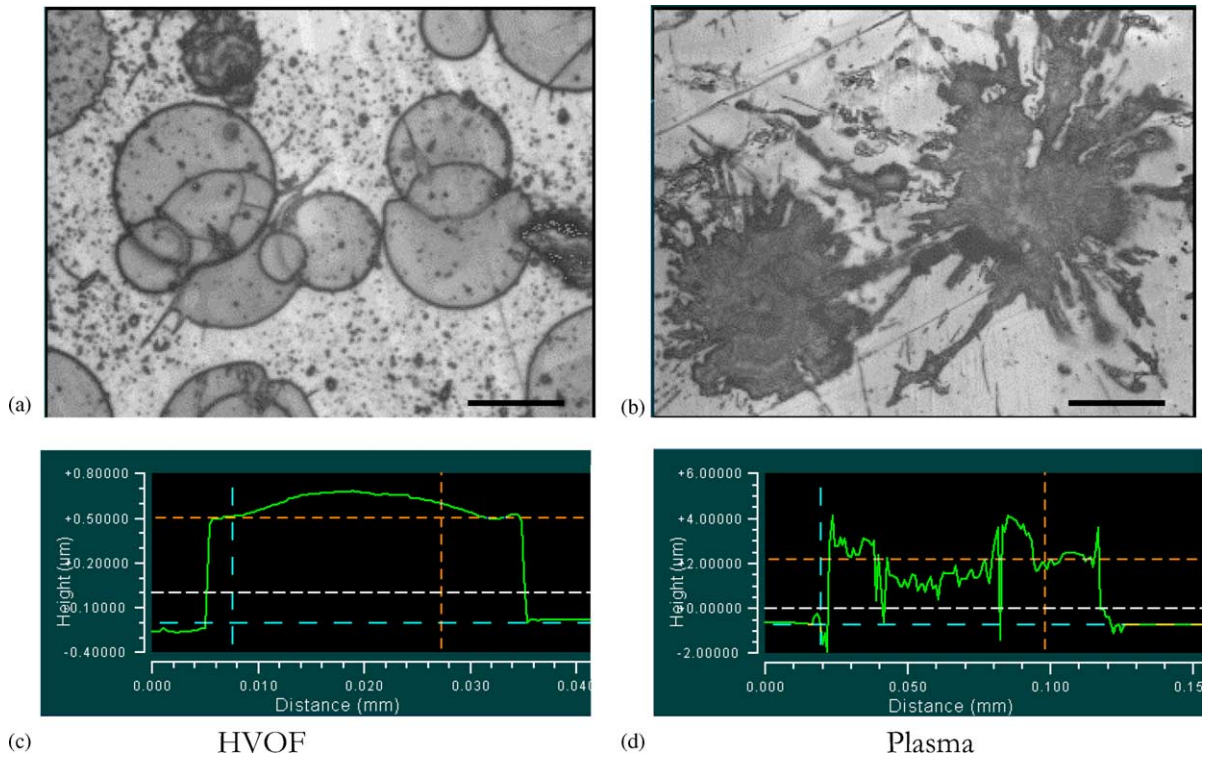

Fig. 4. Single splats (a and b) of HVOF deposited and plasma sprayed alumina. Also shown are their surface profiles (c and d). The splats were collected on polished stainless steel substrates. Thin splats with smooth surface profiles are observed in the HVOF case compared to fragmented/rough-surfaced splat in the case of plasma. The scale bar is 30 μm in figures a and b.

This variation in the nature of the SEM image contrast is unclear. The surface-connected porosity measured by MIP is 4% for HVOF compared to 8% for plasma spray. The lower surface roughness for the top surface of the HVOF coating (compared to plasma spray) results from the use of a finer powder, from enhanced splat flattening, and from the smooth surface of the individual splats collected (Fig. 4).

As shown in Table 4, there is a significant difference in the thermal and mechanical behavior of HVOF and plasma-sprayed coatings. It is seen that, in-spite of higher porosity, the thermal conductivity of the plasma sprayed coating is higher than that for the HVOF coating. It is also observed that the anisotropy in the thermal conductivity is greater for plasma sprayed coating than for HVOF coating. The underlying cause for this is not evident from the SEM micrographs in Fig. 5, where the plasma sprayed coating exhibits distinct pore and crack networks. Therefore, a more detailed microstructure characterization was sought in order to achieve better insight into this apparent anomaly. Unlike the case for thermal conductivity, the elastic modulus values show consistency with the microstructural features observed: as a result of its higher density, the HVOF coating has a larger elastic modulus (in the through-thickness direction) than does the plasma sprayed coating. Also, the anisotropy in the modulus values for plasma spray is negligible as compared to that found for HVOF. However, it is difficult to explain the low in-plane elastic modulus for HVOF. These issues have been further investigated using SANS and CMT.

Table 4
Coating property measurements

Material	Through thickness		In-plane	
	Diffusivity (cm^2/s)	Conductivity (W/m K)	Diffusivity (cm^2/s)	Conductivity (W/m K)
(a) Thermal conductivity				
HVOF	0.014 ± 0.002	3.0 ± 0.2	0.11 ± 0.03	2.4 ± 0.2
Plasma	0.026 ± 0.007	5.1 ± 0.3	0.17 ± 0.01	3.4 ± 0.2
(b) Elastic modulus (GPa)				
HVOF	99 ± 3		70 ± 11	
Plasma	71 ± 9		77 ± 8	

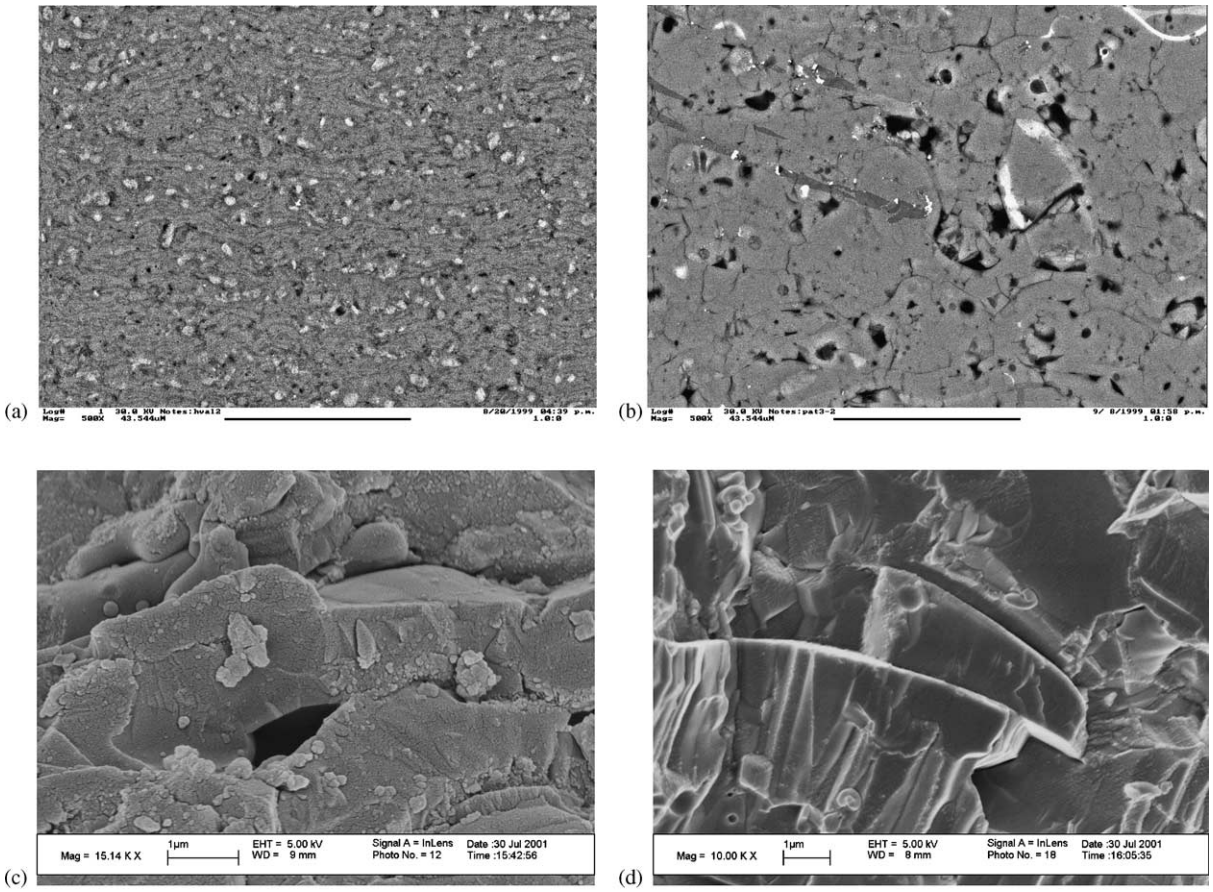

Fig. 5. SEM images of polished (a and b) and fractured (c and d) cross-sections of HVOF deposited and plasma sprayed alumina coatings. The scale-bars represent 45 μm (a and b) and 1 μm (c and d). It is observed that the surface roughness of the HVOF coatings is smoother than the plasma, which can be attributed to the smooth surface profile of the splats shown in Fig. 4.

4. SANS results

SANS results along with the MSANS model fits are presented here. The apparent surface area orientation distributions, derived from the anisotropic variation of the Porod scattering, are shown in Fig. 6, where the orientation dependence of the scatterers is also indicated. Since the scattering associated with a given interface is observed to be perpendicular to the interface plane, the contribution from voids parallel to the substrate is observed along the spray direction, and that from voids or cracks perpendicular to the substrate is observed in in-plane directions. It is observed that the surface area, which is most sensitive to fine features, shows less anisotropy for the case of plasma-spray coatings than that for HVOF coatings. This suggests similar contributions to the surface area from competing networks of cracks and interlamellar pores, respectively, perpendicular and parallel to the substrate. On the other hand, the HVOF coating displays significant anisotropy, attributable to the presence of a layered porosity, parallel to the substrate. Meanwhile, Fig. 7 shows the MSANS broadening data (in units of Q) with the model fits (lines) for the HVOF coating. The figure shows the consistency of the calculated MSANS three-component model results with the experimental data. The objective of MSANS experiments is to determine the broadening of the scattering profiles as a function of the neutron wavelength, which can be used to obtain particle size determinations. This circularly-averaged MSANS broadening, r_c (numerically equal to the curvature of the scattering profile in Q at zero Q, obtained using a Gaussian function] versus λ for the two sample orientations is shown in Fig. 7A and B presents the anisotropic variation of the MSANS r_c parameter averaged over 15° sectors to quantify microstructural anisotropy at different λs, obtained when the incident beam is orthogonal to the spray direction. (The spray direction is the axis of symmetry for the microstructure of either coating.) Comparison of the calculated and measured experimental anisotropy in the MSANS data shows reasonable agreement in the figure.

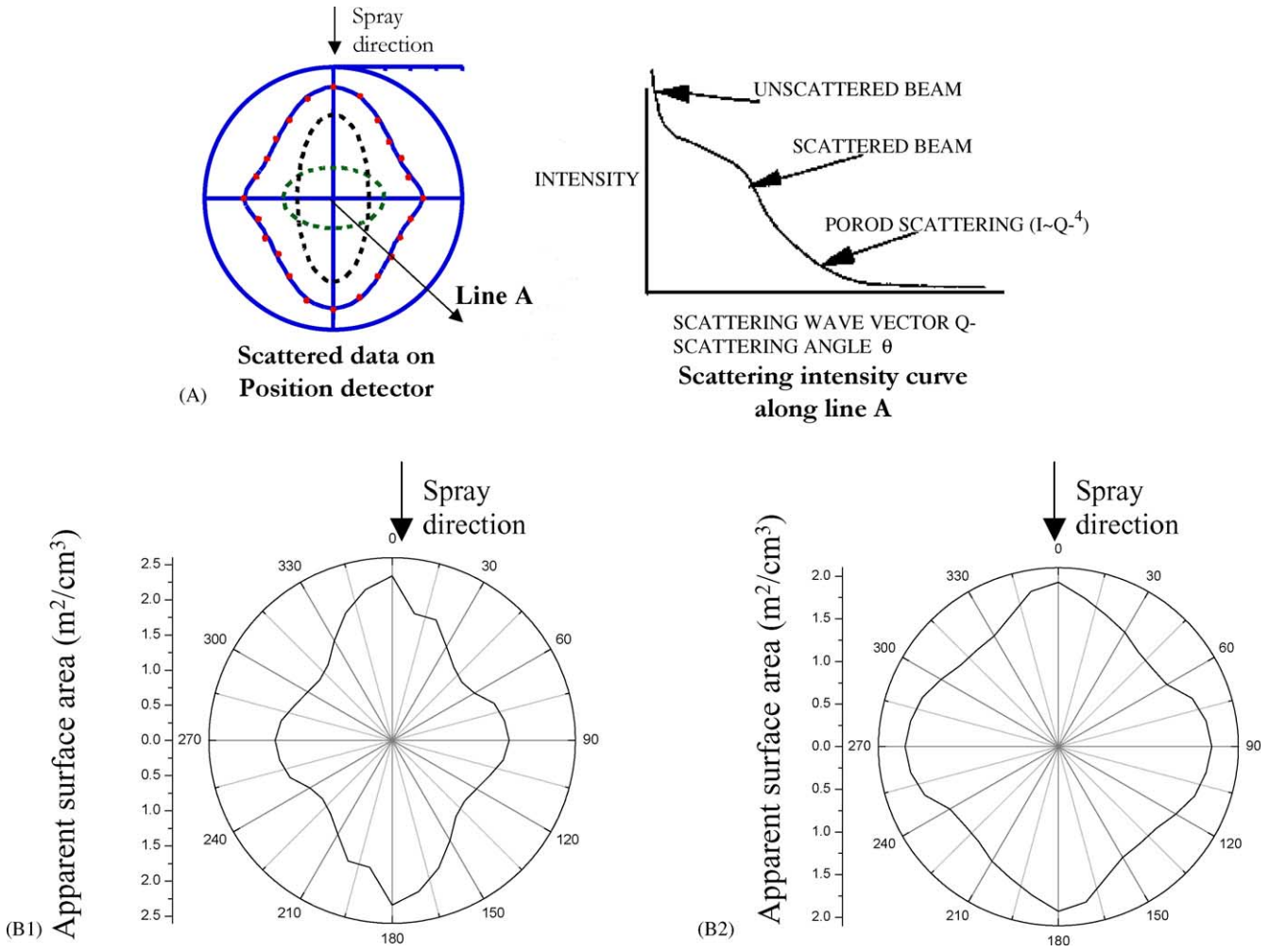

Fig. 6. (A) Anisotropic scattering data along with intensity curve and (B) Porod surface area anisotropy plots for (B1) HVOF deposited and (B2) plasma sprayed alumina coatings.

The overall MSANS model results for the component porosities and mean opening dimensions, along with the estimated standard uncertainties, are summarized in Table 5. To obtain MSANS model fits that satisfy all of the constraints, the intrasplat cracks are found, as expected, to be predominantly perpendicular to the substrate (their spheroidal elements have normals at 60–90° from the spray direction), and the interlamellar pores are found to be predominantly parallel to the substrate (their spheroidal elements have normals at 0–30° from the spray direction). The mean opening dimensions of these anisotropic void systems are reported in Table 5, since it is these dimensions that should pertain to actual cracks and pores within the coating microstructure. The quantitative partitioning of the coating microstructure into its components, obtained from the MSANS model results, is given in Fig. 8. The graph shows that the proportion of interlamellar pores, in the case of the HVOF coating, is some 60% greater than that in the plasma-spray coating. This is probably the underlying cause for the lower thermal conductivity for HVOF.

Table 5
Quantitative MSANS model results

Material	(PD) porosity (%)	Component porosities (%)			Mean opening dimensions (μm)	Globular pore diameter (μm)
		Interlamellar pores	Intrasplat cracks	Globular pores		
Plasma	11.2 ± 0.5	3.8 ± 0.2	3.4 ± 0.2	4.0 ± 0.2	0.070 ± 0.005	0.35 ± 0.04
HVOF	10 ± 0.5	5.5 ± 0.1	3.0 ± 0.5	1.5 ± 0.1	0.084 ± 0.006	0.42 ± 0.05

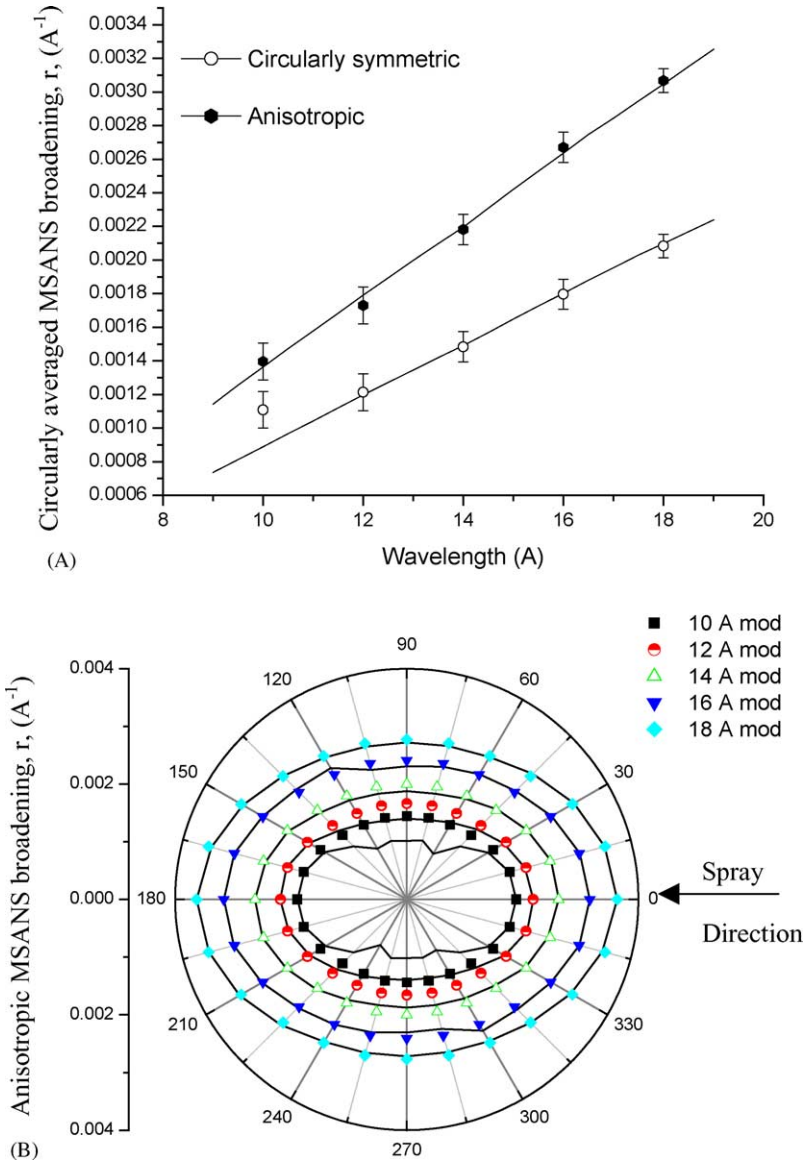

Fig. 7. MSANS broadening experimental data (symbols) with model-fits (lines) for the HVOF alumina coating case: (A) MSANS r_c vs. λ for both the sample orientations; (B) anisotropic angular MSANS, $r_{c,}$ at different wavelengths.

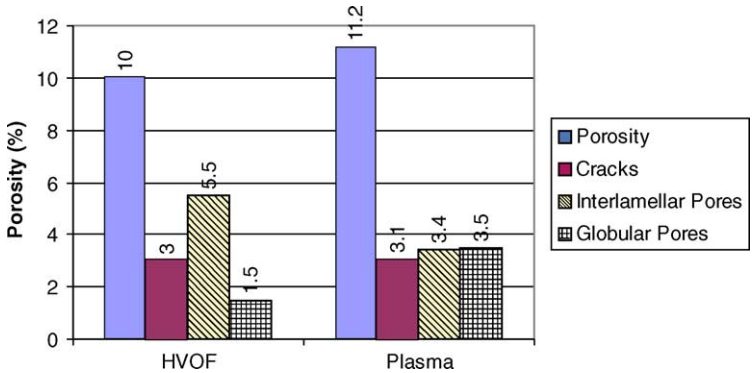

Fig. 8. Quantitative delineation of coating microstructural features.

5. XMT results

The raw data collected as cross-sectional maps are reconstructed using the FFBT algorithm, based on the so-called "Fourier slice" theorem, which is used to generate individual 2D slices. These slices are normalized and centered to generate sinograms (gray scale density maps). These gray scale images depict bimodal peaks in the histogram of the linear attenuation coefficient; one due to the voids and the other due to the solid material. This histogram allows threshold attenuation values to be selected for porosity calculations. The procedure to obtain the results of the 3D medial axis analysis carried out on these images is as follows. Firstly, the 2D images are converted from gray scale density to "black and white" images by a process of segmentation, involving population assignment (material and pores) for each voxel in the image. Since the pore/grain boundary in the image is "fuzzy" due to the finite voxel resolution and

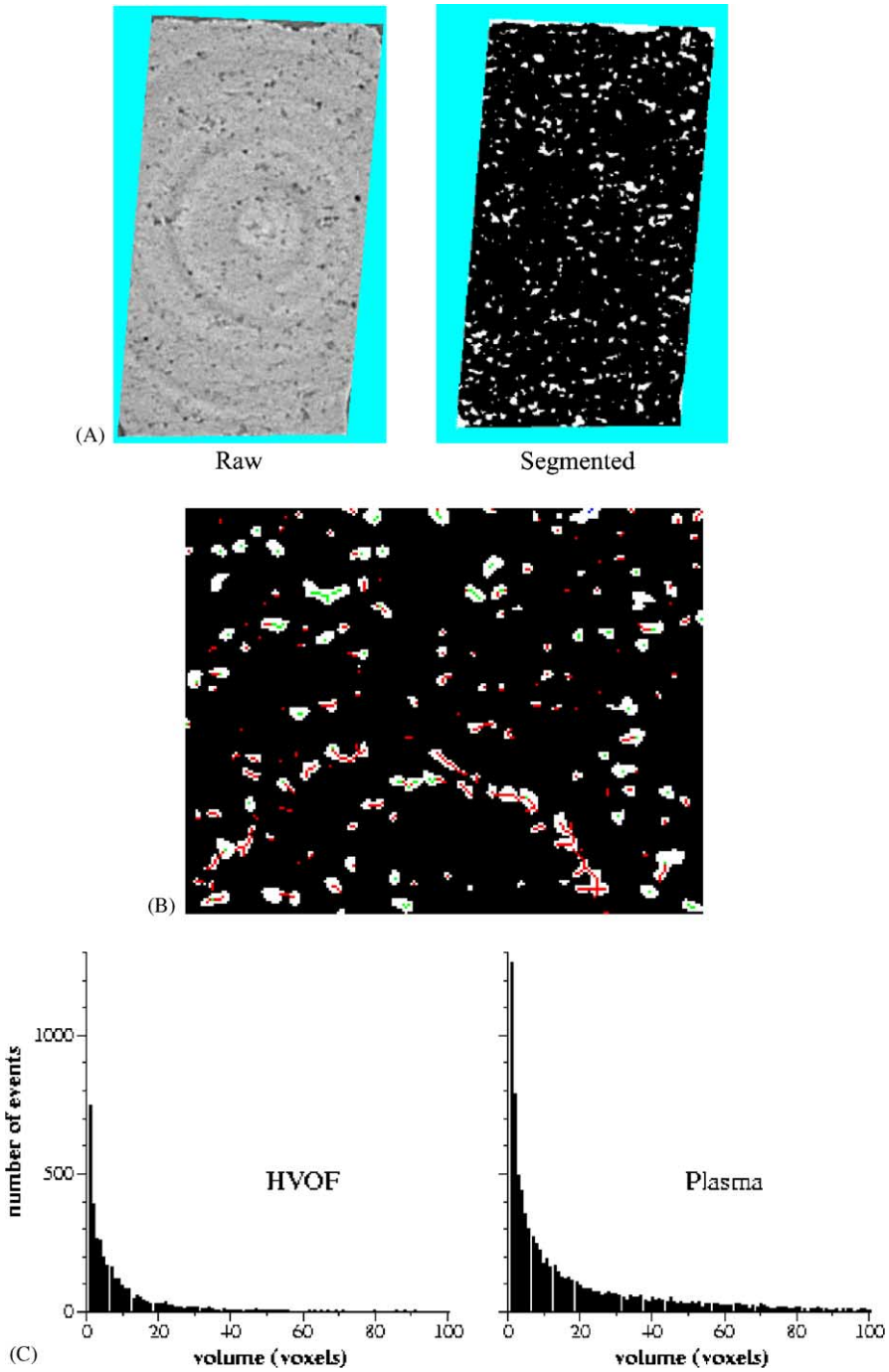

Fig. 9. (A) Raw and reconstructed images along with medial axis computed (B) for a plasma sprayed alumina slice and (C) pore size distributions for the disconnected volumes of HVOF deposited and plasma sprayed alumina coatings.

Table 6
Porosity from MIP and XMT experiments, and from geometric analysis

Material	% Porosity (MIP)	% Porosity (XMT)	Maximum erosion layers	Specific surface area (μm^{-1})
Plasma alumina	8.0 ± 0.4	8.4 ± 0.4	8	0.051 ± 0.070
HVOF alumina	4.0 ± 0.2	4.6 ± 0.3	5	0.021 ± 0.040

image-collection noise, a localized thresholding procedure based on indicator-kriging [29], was used. Fig. 9A shows the raw and segmented images of one slice each for the plasma-sprayed coating. These segmented images are then treated using a mathematical erosion algorithm to construct the medial axis (skeleton) of the void space and to obtain geometric information on the specific surface area and on the distribution of volumes of disconnected components, etc. [26]. Fig. 9B illustrates the medial axis computed for the plasma-sprayed coating. The graph in Fig. 9C shows the size distribution of the disconnected volume components for the two coatings. The size ranges from 1 to 100 voxels, showing the plasma-sprayed coating to have a larger mean pore size than the HVOF coating (1 voxel = 2.7 μm). The porosities, measured by a straight voxel–voxel count over a volume of 100 slices obtained from the segmentation process, are tabulated in Table 6. The somewhat larger porosities in the XMT experiments, compared to the MIP-determined surface connected porosity, are due to the inclusion of both open and closed porosity in XMT. Also shown in the table are the erosion layer sizes (i.e. the relative number of voxels at each discrete distance normal to the void surface) for each coating, as well as the specific surface area, estimated by a voxel face count.

Fig. 10 shows microstructural features in the plasma-sprayed and HVOF coatings using a 3D representation where the void space is displayed as transparent. The figures reveal a predominant globular porosity for plasma-sprayed and layered porosity for HVOF. The ring artifact is due to drifts or non-linearities in the detector response combined with position registration errors on rotating the sample. The artifacts can be removed through the use of a numerical algorithm [30], but this was not done here. Fig. 10B also shows the pore morphology in plasma-sprayed and HVOF-deposited coatings. Here, the grain structure is displayed as the transparent phase, more clearly revealing the pore connectivity. The plasma-spray coating shows few connected pores, whereas the HVOF coating displays significant layered porosity, which is clearly revealed as the underlying basis for the lower thermal conductivity exhibited by HVOF coatings.

Further effects of the layered porosity in HVOF coatings were apparent in preliminary indentation studies carried out at high loads. Fig. 11A shows large cracks propagating horizontally through the coating, indicating that the adhesion is considerably poorer at these locations than elsewhere. These weak layers can be associated with the inter-pass interfaces during the coating development, where the deposition rate

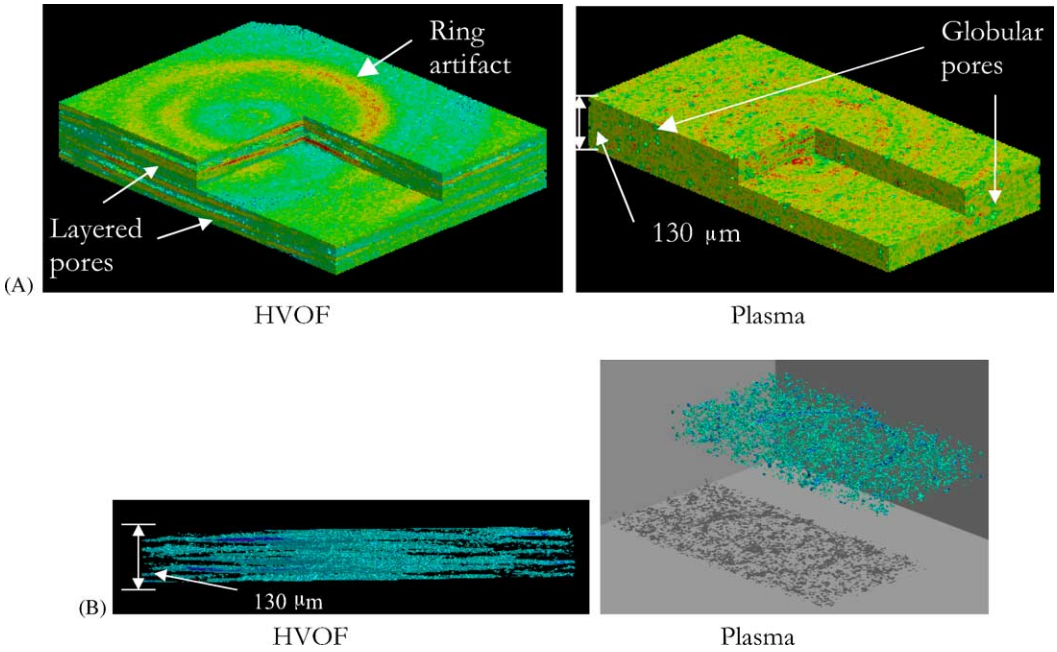

Fig. 10. (A) 3D visualizations from volume rendering of 50 slices in each coating and (B) pore morphology observed in sprayed coatings.

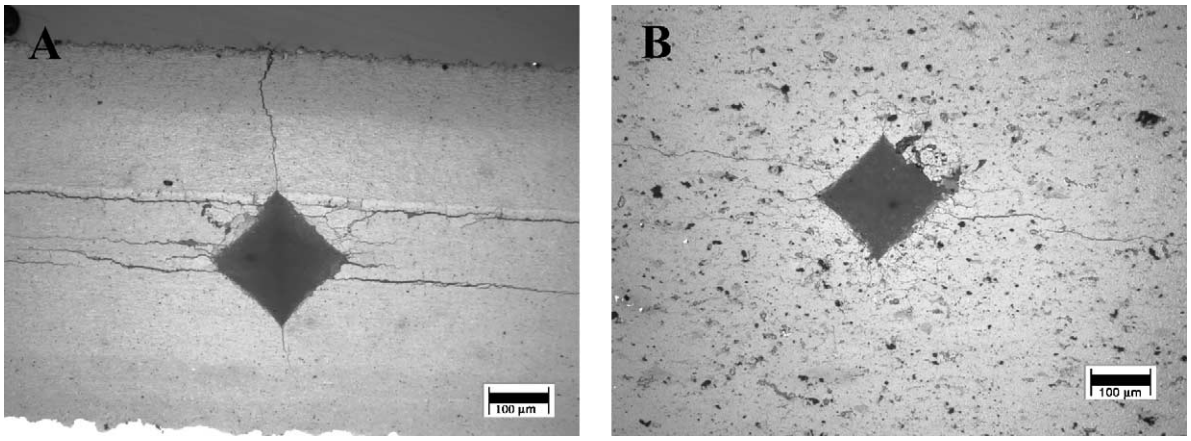

Fig. 11. High load indentation studies on (A) HVOF deposited and (B) plasma sprayed coatings showing existence of layered porosity in HVOF coating. Scale bar is 100 μm in each case.

is 25 μm/pass during processing. This layered structure is further accentuated by the large flattening ratio and smooth surface of the splats, which can lower the adhesion in the interpass region. In contrast, the interlamellar-pore tortuosity is significantly larger for the low velocity plasma-sprayed coatings, as shown in Fig. 11B.

6. Conclusions

This paper confirms that the HVOF process can be used to deposit alumina-based ceramics to produce dense, well-adhered coatings. Multidisciplinary approaches towards material microstructure characterization have made possible an explanation of the observed porosity—property correlations. While SANS studies provide microstructure information for the constituent porosities, opening dimensions, and orientation distributions of the void components, the XMT results reveal the differences in the larger-scale void morphology arising from differences in the thermal spray process: i.e. predominantly globular porosity in plasma-spray, highly layered porosity in HVOF. It can be concluded that high density, high through-thickness elastic modulus, and an absence of interconnected pore/crack structures, indicate that HVOF ceramic coating technology offers considerable promise for coating applications in extreme wear and corrosion environments, as well as in functional thick films.

Acknowledgements

This work was sponsored in part by the MRSEC program of the National Science Foundation under award DMR-0080021. This work utilized facilities supported in part by the National Science Foundation under Agreement No. DMR-9986442. We acknowledge the support of the National Institute of Standards and Technology, US Department of Commerce, in providing the neutron research facilities used in this work.

References

[1] P. Chagnon, P. Fauchais, Ceram. Int. 10 (4) (1984) 119.
[2] R.A. Zatorski, H. Herman, in: P. Vincenzini (Ed.), High Performance Ceramic Films and Coatings, Elsevier, 1991, p. 591.
[3] D. Chuanxian, R.A. Zatorski, H. Herman, Thin Solid Films 118 (1984) 467.
[4] W. Mannsmann, H.W. Grunling, J. Phys. IV 3 (1993) 903.
[5] H. Herman, Sci. Am. 259 (3) (1987) 112.
[6] L. Pawlowski, P. Fauchais, Int. Metall. Rev. 37 (6) (1992) 271.
[7] R. McPherson, Silikaty 35 (1991) 273.
[8] D.C. Crawmer, J.D. Krebsback, W.L. Riggs, in: Proceedings of the ITSC, 1992, p. 127.
[9] K.A. Kowalsky, D.R. Marantz, M.F. Smith, W.L. Oberkampf, in: Proceedings of the 3rd NTSC, 1990, p. 20.
[10] M.L. Thorpe, H.J. Richter, J. Therm. Spray Technol. 1 (2) (1992) 161.
[11] A.J. Sturgeon, M.D.F. Harvey, F.J. Blunt, S.B. Dunkerton, in: Proceedings of the 14th ITSC, 1995, p. 669.
[12] Y. Shimizu, K. Sugiura, K. Sakaki, A. Devasanapathi, in: Proceedings of the UTSC, 2000, p. 181.
[13] J. Ilavsky, A.J. Allen, G.G. Long, S. Krueger, C.C. Berndt, H. Herman, J. Am. Ceram. Soc 80 (1997) 733.
[14] A.J. Allen, J. Ilavsky, G.G. Long, J.S. Wallace, C.C. Berndt, H. Herman, Acta Mater. 49 (2001) 1661.
[15] H. Boukari, A.J. Allen, G.G. Long, J. Ilavsky, J.S. Wallace, C.C. Berndt, H. Herman, J. Mater. Res. 18 (3) (2003) 624.
[16] A. Kulkarni, S. Sampath, A. Goland, B. Dowd, H. Herman, Scripta Mater. 43 (2000) 471.
[17] W.J. Parker, R.J. Jenkins, C.P. Butler, G.L. Abbott, J. Appl. Phys. 32 (9) (1961) 1679.
[18] A.B. Donaldson, R.E. Taylor, J. Appl. Phys. 46 (1975) 4584.
[19] W.C. Oliver, G.M. Pharr, J. Mater. Res. 7 (6) (1992) 1564.
[20] C.J. Glinka, J.M. Rowe, J.G. LaRock, J. Appl. Cryst. 19 (1985) 427.
[21] B. Hammouda, S. Krueger, C.J. Glinka, J. Res. Natl. Inst. Stand. Technol. 98 (1993) 31.
[22] B.A. Dowd, A.B. Andrews, R.B. Marr, D.P. Siddons, K.W. Jones, A.M. Peskin, Advances in X-ray Analysis, 1999, p. 42.
[23] B.A. Dowd, G.H. Campbell, R.B. Marr, V. Nagarkar, S. Tipnis, L. Axe, D.P. Siddons, in: Proceedings of the SPIE, 1999, p. 3772.

[24] P. Spanne, J.F. Thovert, C.J. Jacquin, W.B. Lindquist, K.W. Jones, P.M. Adler, Phys. Rev. Lett. 73 (1994) 2001.
[25] T.C. Lee, R.L. Kashyap, C.N. Chu, CVGIP: Graph. Models Image Process. 56 (1994) 462.
[26] W.B. Lindquist, S.M. Lee, D.A. Coker, K.W. Jones, P. Spanne, J. Geophys. Res. 101 (B4) (1996) 8297.
[27] W.B. Lindquist, A.B. Venkatarangan, J.H. Dunsmuir, T.F. Wond, J. Geophys. Res. 105B (2000) 21508.
[28] http://www.ccp14.ac.uk/tutorial/powder.
[29] W. Oh, W.B. Lindquist, IEEE Trans. Patt. Anal. Mach. Intell. 21 (1999) 590.
[30] C. Raven, Rev. Sci. Instrum. 69 (8) (1998) 2978.